

Magnetic trapping caused by resonant perturbations in tokamaks with reversed magnetic shear

Marisa Roberto

Instituto Tecnológico de Aeronáutica, Centro Técnico Aeroespacial, Departamento de Física, 12228-900, São José dos Campos, São Paulo, Brazil

Elton C. da Silva and Iberê L. Caldas

Instituto de Física, Universidade de São Paulo 05315-970, São Paulo, São Paulo, Brazil

Ricardo L. Viana

Departamento de Física, Universidade Federal do Paraná, 81531-990, Curitiba, Paraná, Brazil

(Received 31 March 2003; accepted 7 October 2003)

Reversed magnetic shear configurations in tokamaks reduce substantially particle diffusivity and improve plasma confinement due to the formation of a transport barrier, as a result of magnetic field line reconnection and bifurcation. The latter are caused by the resonant perturbation of an ergodic limiter on a tokamak with reversed magnetic shear, which creates a region with chaotic field lines in the vicinity of the dimerized island chains. An analytically derived nontwist map for field lines is used to describe the formation of a transport barrier, manifested in the decrease of field line diffusion rate. This barrier appears due to the chaotic field line trapping near the reconnection layer that survives the bifurcation. © 2004 American Institute of Physics. [DOI: 10.1063/1.1630318]

I. INTRODUCTION

The recently discovered fact that a negative magnetic shear can enhance substantially plasma confinement in tokamaks has started an intensive investigation of such configurations.^{1–3} A negative magnetic shear for some portion of the plasma column implies a nonmonotonic radial profile for the safety factor which, on its hand, can be produced by a nonpeaked plasma current density. Since inductive current drive is most likely to generate peaked current profiles, nonpeaked ones are possible by noninductive methods like neutral beam injection. The combination of heating and current drive by such method has been proved to generate configurations with enhanced reversed shear (ERS) in the plasma startup phase, with highly peaked density and pressure profiles.^{1–3}

Among the advantages of producing plasma discharges with reversed magnetic shear we cite the following ones: (i) a high fraction of the self-sustained bootstrap current aligned with an optimized current density profile; (ii) certain micro-instabilities responsible for anomalous electron transport can be stabilized, as well as some magnetohydrodynamical (MHD) modes (ballooning and resistive tearing); and (iii) it has been observed in transitions from low (L) to high (H) mode discharges.⁴ There has been observed a reduction of the plasma transport in the central region of the plasma column, through the formation of a transport barrier, or a region where both the electron and ion diffusivities are greatly reduced around the shearless region.

A theoretical interpretation for the formation of a transport barrier can be built upon a configuration with reversed magnetic shear perturbed by internal resonant magnetic perturbation as well as by external helical windings that have been used to control plasma oscillations.⁵ The field line

structure produced by such a configuration is suitably described by a nontwist area-preserving map, in which a single perturbation mode can excite the formation of twin dimerized island chains. Properties of nontwist maps have been extensively studied, from the mathematical and applied points of view.^{6–8} Nontwist maps violate the nondegeneracy condition for the Kolmogorov–Arnold–Moser (KAM) theorem to be valid, so that many well-known results of canonical mappings no longer apply to them.⁹ For example, it may happen that two neighbor island chains approach each other without being destroyed through the breakup of KAM curves. Detailed studies have been carried out in order to understand the transition to chaos in nontwist maps, involving a combination of analytical and numerical methods.^{6–8}

In fact, nontwist maps have been proposed to investigate the effect of reversed shear in tokamak confinement.^{10,11} The map we have used in this paper, on the other hand, has parameters directly related to physical quantities characterizing tokamak equilibrium and perturbation fields. Hence, our map may be used in a conceptual project of such an experiment. Moreover, we can vary the perturbation amplitude in order to study how it affects plasma equilibria experimentally observed in tokamaks.

The transport barrier of interest to plasma confinement arises from a combination of typical features of nontwist maps: reconnection and bifurcation, occurring in the reversed shear region. Reconnection in a chaotic region of a nontwist map has been described by Corso and Rizzato,¹² who showed that diffusion increases after a smooth manifold reconnection in a chaotic regime. This provides the framework to study a transport barrier in reversed shear configurations perturbed by nonintegrable magnetic fields which can generate field line chaos. Analyses of the formation of a barrier transport in reversed shear configurations usually take

into account the effect of internal instabilities that ergodize some portion of the plasma column.^{13,14} In this paper, however. We shall intentionally create an outer chaotic layer of magnetic field lines. We have superimposed to the tokamak equilibrium field the magnetic field generated by an ergodic magnetic limiter (EML), which consists of slices of external helical conductors with a suitable pitch.^{15,16} It is generally thought that this cold boundary layer is able to spread heat and particle loadings on the tokamak inner wall, so reducing plasma contamination by impurities released from the vessel wall by sputtering processes, for example.^{16,17} The properties of such an external device have been extensively studied using field line maps since the seminal work of Martin and Taylor.¹⁸ Such ergodic limiters have been used to control plasma instabilities and improve plasma parameters in some tokamaks, as in TEXTOR,¹⁹ TEXT (Texas Experimental Tokamak),²⁰ TORE-SUPRA,²¹ and TBR (Brazilian Tokamak).²²

We use an analytical approach to this problem by considering a convenient coordinate system in which the Grad–Schlüter–Shafranov equation can be solved in an approximated way.^{23,24} Moreover, a perturbation magnetic field from an ergodic magnetic limiter is chosen in such a way that the integrability of the field line configuration is broken and Lagrangian chaos is possible. This enables us to analytically derive a Poincaré map.²⁵ The area-preserving nature of this map comes from neglecting of any dissipative effects in the plasma, so that the mentioned field line reconnection is not due to a resistive layer. This map can be used to numerically evidence the formation of a transport barrier due to a reconnection–bifurcation mechanism, and its effect on the plasma transport can be inferred from the study of field line diffusion by using the obtained map. The transport barrier we obtain is effective for a limited time span, since the chaotic region generated by a limiter reaches the tokamak wall, such that field lines are eventually lost due to radial diffusion and ultimate collision with the wall. However, as a consequence of island reconnection and bifurcation, field lines are effectively trapped due to the stickiness effect of the magnetic islands, provided the duration of a discharge is less than the average escape time.

The rest of this paper is organized as follows: in Sec. II we present the model fields for the reversed shear equilibrium and the ergodic limiter perturbation, and an analytically obtained field line mapping. Section III analyzes the reconnection and bifurcation processes involved when the limiter current is increased past critical values. Section IV presents an analytical treatment for the widths of the dimerized island chains, in order to estimate the threshold perturbation for field line reconnection. The transport barrier, which appears as the result of the reconnection, and the underlying manifold structure, are treated in Sec. V. Our conclusions are left to the last section.

II. EQUILIBRIUM AND PERTURBING MAGNETIC FIELDS

Many coordinate systems have been used to describe magnetic field line geometry in plasma confinement systems.

One of them is the toroidal coordinates (ξ, ω, Φ) ,²⁶ defined in terms of the circular–cylindrical coordinates (R, φ, Z) by

$$R = \frac{R'_0 \sinh \xi}{\cosh \xi - \cos \omega}, \quad Z = \frac{R'_0 \sin \omega}{\cosh \xi - \cos \omega}, \quad (1)$$

where R'_0 is the major radius of the circular center (i.e., the magnetic axis radius). In this coordinate system ω has the meaning of a poloidal angle, and ξ is related to the distance from the circular center.

Throughout this paper, however, we will work with the following non-orthogonal coordinates: $(r_t, \theta_t, \varphi_t)$, given by²⁴

$$r_t = \frac{R'_0}{\cosh \xi - \cos \omega}, \quad \theta_t = \pi - \omega, \quad \varphi_t = \Phi, \quad (2)$$

which are related to the local (or pseudotoroidal) coordinates (r, θ, φ) by the following relations:

$$r_t = r \left[1 - \frac{r}{R'_0} \cos \theta + \left(\frac{r}{2R'_0} \right)^2 \right]^{1/2}, \quad (3)$$

$$\sin \theta_t = \sin \theta \left[1 - \frac{r}{R'_0} \cos \theta + \left(\frac{r}{2R'_0} \right)^2 \right]^{-1/2}, \quad (4)$$

such that, in the large aspect ratio limit ($r_t \ll R'_0$), r_t and θ_t become r and θ , respectively. Note that the origins of these two coordinate systems are the magnetic axis. Finally, the relation of the magnetic axis radius R'_0 with the approximate radius \bar{R} is

$$\bar{R}^2 = R_0'^2 \left[1 - 2 \frac{r_t}{R'_0} \cos \theta_t - \left(\frac{r_t}{R'_0} \right)^2 \sin^2 \theta_t \right]. \quad (5)$$

The tokamak equilibrium magnetic field \mathbf{B}_0 is obtained from an approximated analytical solution of the Grad–Schlüter–Shafranov equation in these coordinates.²⁴

$$\Psi_p(r_t, \theta_t) = \Psi_{p0}(r_t) + \delta\Psi_p(r_t, \theta_t), \quad (6)$$

where

$$\frac{d\Psi_{p0}(r_t)}{dr_t} = \frac{\mu_0 I_p R'_0}{2\pi r_t} \left[1 - \left(1 + \beta' \frac{r_t^2}{a^2} \right) \left(1 - \frac{r_t^2}{a^2} \right)^{\gamma+1} \right], \quad (7)$$

with a as the plasma radius, determined by a material limiter, $\beta' \equiv \beta(\gamma+1)/(\beta+\gamma+2)$, where β and γ are positive parameters, and $|\delta\Psi_p(r_t, \theta_t)| \ll |\Psi_{p0}(r_t)|$.

In the large aspect ratio limit, and supposing that in lowest order the equilibrium flux function $\Psi_p(r_t)$ does not depend on θ_t , the Grad–Schlüter–Shafranov equation reduces to an equilibrium equation similar to that obtained in a cylindrical system, but now in terms of r_t . This has been our main motivation to work with the $(r_t, \theta_t, \varphi_t)$ coordinate system. The intersections of the flux surfaces $\Psi_p(r_t) = \text{constant}$ with a toroidal plane are not concentric circles but rather present a Shafranov shift toward the exterior equatorial region. Hence, actual equilibrium flux surfaces can be approximated by $r_t = \text{constant}$ coordinate surfaces. In the common range of tokamak parameters, as those considered in this paper, the aspect ratio is always large enough to ensure that the $r_t = \text{constant}$ surfaces do not overlap.

Moreover, from Eq. (5), there results that, in order to avoid imaginary values of the \bar{R} coordinate, the inverse local aspect ratio r_t/R'_0 should not exceed 1/2. In fact, this condition is always fulfilled with the parameter values used in this paper, if the inverse aspect ratio at the plasma edge satisfies $a/R'_0 < 1/2$, as is commonly found in present tokamaks. However, it must be mentioned that for other magnetic configurations, like compact tori or spheromaks, this condition might not be fulfilled for all points in the plasma and the $r_t = \text{constant}$ surfaces may overlap, spoiling their use as good equilibrium flux surfaces.

We have used a toroidal current density profile with a central hole, given by²⁷

$$J_3(r_t) = \frac{I_p R'_0}{\pi a^2} \frac{(\gamma+2)(\gamma+1)}{\beta+\gamma+2} \left(1 + \beta \frac{r_t^2}{a^2}\right) \left(1 - \frac{r_t^2}{a^2}\right)^\gamma, \quad (8)$$

where I_p is the total plasma current.

In this MHD equilibrium, the contravariant components of the equilibrium field are given by

$$B_0^1 = -\frac{1}{R'_0 r_t} \frac{\partial \Psi_p}{\partial \theta_t} = 0, \quad (9)$$

$$B_0^2(r_t) = \frac{1}{R'_0 r_t} \frac{\partial \Psi_p}{\partial r_t} = \frac{\mu_0 I_p}{2\pi r_t^2} \left[1 - \left(1 + \beta' \frac{r_t^2}{a^2}\right) \left(1 - \frac{r_t^2}{a^2}\right)^{\gamma+1}\right], \quad (10)$$

$$B_0^3(r_t, \theta_t) = -\frac{\mu_0 I}{\bar{R}^2} = \frac{\mu_0 I_e}{2\pi R'_0{}^2} \left[1 - 2 \frac{r_t}{R'_0} \cos \theta_t\right]^{-1}, \quad (11)$$

where $I_e \approx -I/2\pi$ is the total current in the toroidal field coils in the large aspect ratio approximation. There results that the safety factor of the magnetic surfaces,

$$q(r_t) = \frac{1}{2\pi} \int_0^{2\pi} \frac{B_0^3(r_t, \theta_t)}{B_0^2(r_t)} d\theta_t, \quad (12)$$

has a nonmonotonic profile, which accounts for describing the reversed shear effect. For some values of the safety factor there are two magnetic surfaces with different radii within the plasma column. Such nonmonotonic profiles can trigger double tearing mode instabilities,¹⁴ and have been observed in initial stages of tokamak discharges,¹³ as well as in transitions from L to H mode discharges.³

In the numerical simulations to be described in this paper, we normalize the minor tokamak radius b_t , and the plasma radius a to the major (magnetic axis) radius R'_0 , such that $a/R'_0 = 0.25$ and $b/R'_0 = 0.33$.²⁵ We also choose $q(a) = 4.04$ and $q(0) = 3.50$, corresponding to the safety factors at the plasma edge and magnetic axis, respectively, as observed in typical discharges with negative magnetic shear, for which $\beta = 3.0$ and $\gamma = 1.0$. Figure 1(a) shows some equilibrium flux surfaces for this set of parameters, and Fig. 1(b) depicts the corresponding radial profile of the safety factor (12) (solid line). For comparison, a usual monotonic radial profile for $q(0) = 1.25$ and the same value of $q(a) = 4.04$ is also shown in Fig. 1(b).

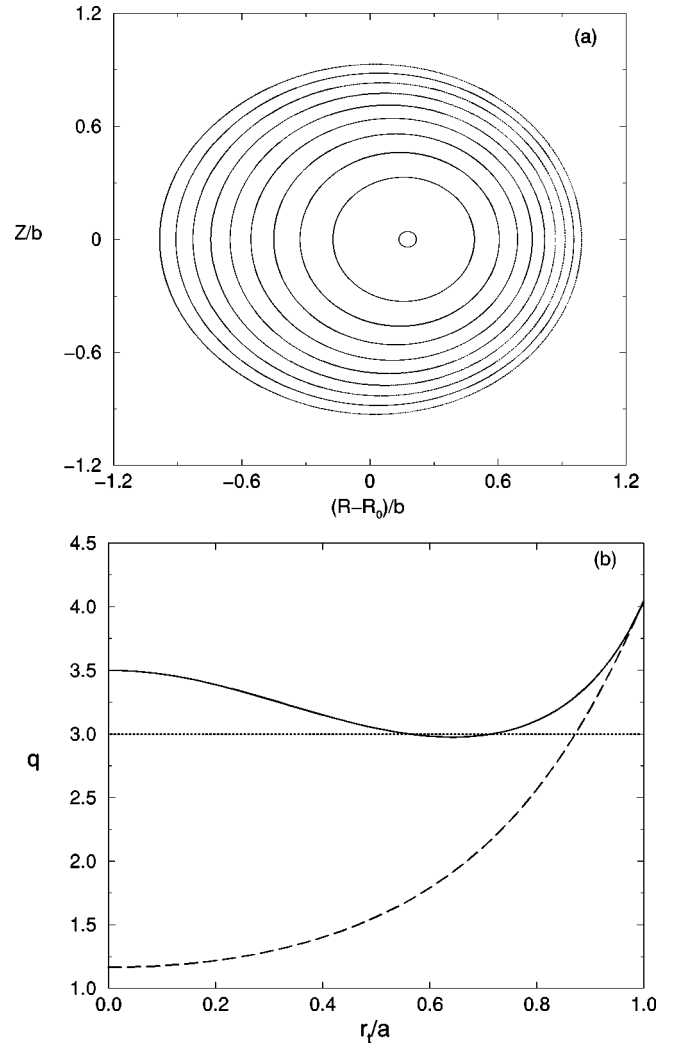


FIG. 1. (a) Flux surfaces for a reversed shear equilibrium with parameters $\beta = 3.0$ and $\gamma = 1.0$; (b) safety factor profile for equilibria with $\gamma = 1.0$, $\beta = 3.0$ (solid line), and $\gamma = 2.0$, $\beta = 0.0$ (dashed line). The minor radius of tokamak vessel is denoted by b .

The design for the ergodic magnetic limiter to be considered in this paper is essentially the same as in Ref. 25, and consists of N_r current rings of length ℓ located symmetrically along the toroidal direction of the tokamak (Fig. 2). These current rings may be regarded as slices of a pair of external helical windings located at $r_t = b_t$, conducting a current I_h in opposite senses for adjacent conductors. The role of these windings is to induce a resonant perturbation in the tokamak, and to achieve this effect we must choose a helical winding with the same pitch as the field lines in the rational surface we want to perturb. This has been carried out by choosing the following winding law²⁵ $u_t = m_0 \theta_t - n_0 \varphi_t = \text{constant}$. In this paper we will consider an ergodic limiter consisting of $N_r = 4$ rings with mode numbers $(m_0, n_0) = (3, 1)$ each, carrying a current I_h .

The magnetic field \mathbf{B}_L produced by the resonant helical winding, from which we build the EML rings, is obtained by neglecting the plasma response and the penetration time through the tokamak wall. In this case, \mathbf{B}_L is assumed to be a vacuum field, such that it comes from solving Laplace's

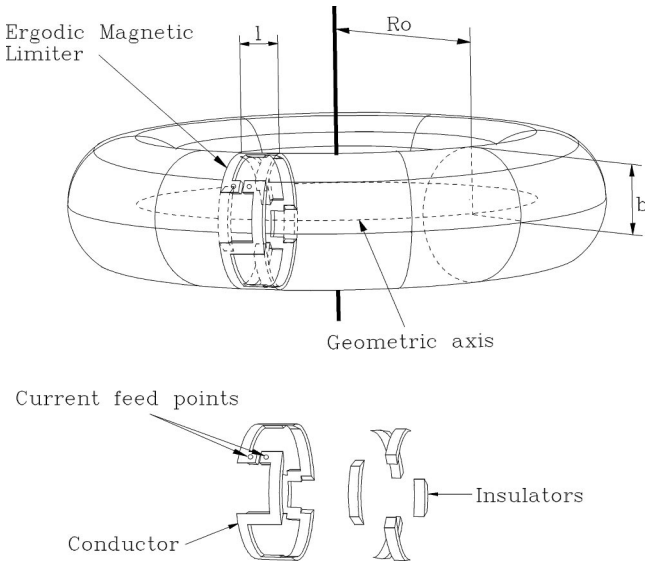


FIG. 2. Scheme and exploded view of an ergodic magnetic limiter.

equation with proper boundary conditions at the tokamak wall. We were able to obtain an approximated analytical solution, such that, in lowest order, the only nonvanishing component of the corresponding vector potential is²⁵

$$A_{L3}(r_t, \theta_t, \varphi_t) = -\frac{\mu_0 I_h R_0'}{\pi} \left(\frac{r_t}{b_t} \right)^{m_0} \cos(m_0 \theta_t - n_0 \varphi_t). \quad (13)$$

The model field to be used in this paper will be the superposition of the equilibrium and limiter fields: $\mathbf{B} = \mathbf{B}_0 + \mathbf{B}_L$, with the corresponding magnetic field line equations:

$$\frac{dr_t}{d\varphi_t} = -\frac{1}{r_t B_T} \left(1 - 2 \frac{r_t}{R_0'} \cos \theta_t \right) \frac{\partial}{\partial \theta_t} A_{L3}(r_t, \theta_t, \varphi_t), \quad (14)$$

$$\begin{aligned} \frac{d\theta_t}{d\varphi_t} &= \frac{1}{r_t B_T} \left(1 - 2 \frac{r_t}{R_0'} \cos \theta_t \right) \\ &\times \frac{\partial}{\partial r_t} [\Psi_{p0}(r_t) + A_{L3}(r_t, \theta_t, \varphi_t)], \end{aligned} \quad (15)$$

where B_T is the toroidal magnetic field at the magnetic axis.

Since the equilibrium field is axisymmetric, we may set the azimuthal angle, $\varphi_t = t$, as a time-like variable, and put field line Eqs. (14) and (15) in a Hamiltonian form,

$$\frac{d\mathcal{J}}{dt} = -\frac{\partial H}{\partial \vartheta}, \quad \frac{d\vartheta}{dt} = \frac{\partial H}{\partial \mathcal{J}}, \quad (16)$$

where (\mathcal{J}, ϑ) are the action-angle variables of a Hamiltonian H , which can be found in the Appendix [Eqs. (A1)–(A11)].

The addition of the magnetic field produced by a resonant helical characterized by Eq. (13) may be regarded as a Hamiltonian perturbation

$$H(\mathcal{J}, \vartheta, t) = H_0(\mathcal{J}) + H_1(\mathcal{J}, \vartheta, t), \quad (|H_1/H_0| \ll 1) \quad (17)$$

$$= \frac{1}{B_T R_0'^2} \Psi_{p0}(\mathcal{J}) + \frac{1}{B_T R_0'^2} A_{L3}(\mathcal{J}, \vartheta, t). \quad (18)$$

In order to include the effect of the finite length ℓ of each EML ring, which is typically a small fraction of the total toroidal circumference $2\pi R_0'$, we model its effect as a sequence of delta-functions centered at each ring position:²⁸

$$H_L(\mathcal{J}, \vartheta, t) = H_0(\mathcal{J}) + \frac{\ell}{R_0'} H_1(\mathcal{J}, \vartheta, t) \sum_{k=-\infty}^{+\infty} \delta\left(t - k \frac{2\pi}{N_r}\right), \quad (19)$$

where the N_r rings are symmetrically distributed in the toroidal direction. This assumption is consistent with results obtained using full numerical codes for generating the field line map by directly computing the magnetic field of a finite-sized limiter, and which point out that the limiter influence is actually concentrated in a small region.¹⁹

We can derive, due to the impulsive perturbation, a stroboscopic map for field line dynamics, by defining \mathcal{J}_n and ϑ_n as the action and angle variables just after the n th kick due to a limiter ring at the toroidal positions $\varphi_k = 2k\pi/N_r$, with $k = 0, 1, \dots, N_r - 1$.²⁹

$$\mathcal{J}_{n+1} = \mathcal{J}_n + \epsilon f(\mathcal{J}_{n+1}, \vartheta_n, t_n), \quad (20)$$

$$\vartheta_{n+1} = \vartheta_n + \frac{2\pi}{N_r q(\mathcal{J}_{n+1})} + \epsilon g(\mathcal{J}_{n+1}, \vartheta_n, t_n), \quad (21)$$

$$t_{n+1} = t_n + \frac{2\pi}{N_r}, \quad (22)$$

where

$$f(\mathcal{J}, \vartheta, t) = -\frac{\partial H_1(\mathcal{J}, \vartheta, t)}{\partial \vartheta}, \quad g(\mathcal{J}, \vartheta, t) = \frac{\partial H_1(\mathcal{J}, \vartheta, t)}{\partial \mathcal{J}}, \quad (23)$$

and the perturbation parameter is

$$\epsilon = -2 \left(\frac{\ell}{2\pi R_0'} \right) \left(\frac{I_h}{I} \right), \quad (24)$$

which is usually small, since in experiments we have $\ell \ll 2\pi R_0'$ and $I_h \ll I$. A more detailed form of the above functions can be found in the Appendix.

III. RECONNECTION AND BIFURCATION

The phase portraits generated by the ergodic limiter map correspond, in the action-angle variables (\mathcal{J}, ϑ) , to a Poincaré surface of section at fixed $t = \varphi = 0$, where we plot a large number of points corresponding to different initial conditions spread over the radial extension of the toroidal chamber. In Figs. 3(a) to 3(c) we show phase portraits, for different values of the limiter current, representatives of the situations to be discussed in this section. Since we have chosen a limiter with $m_0 = 3$ pairs of current wires, its perturbing field

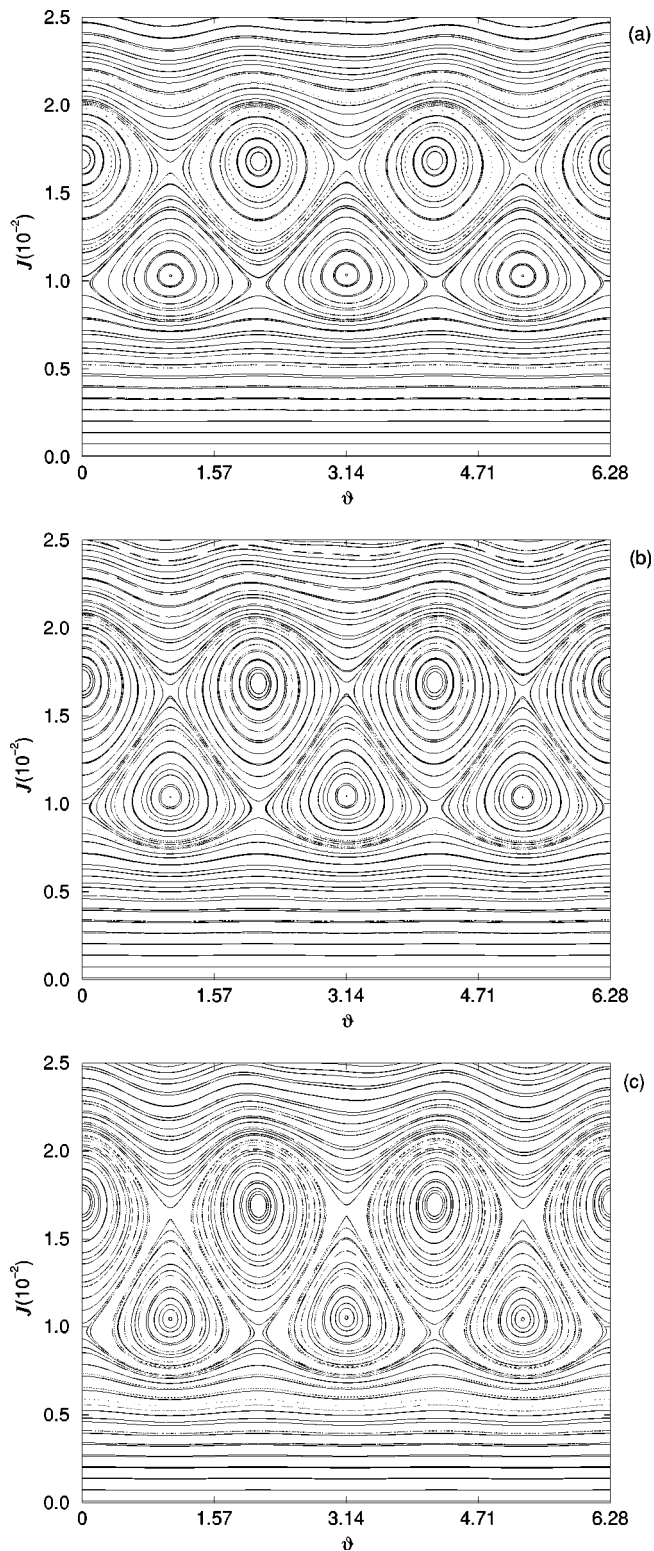


FIG. 3. Poincaré maps for the ergodic limiter mapping, an equilibrium with $\beta=3.0$ and $\gamma=1.0$, and normalized limiter currents $I_h/I_p=(a)$ 0.86%, (b) 1.15%, and (c) 1.39%, respectively before, during, and after reconnection.

resonates with the equilibrium tokamak field and generates chains of three magnetic islands. Since the safety factor radial profile is non-monotonic, for $q=3.0$ there are two distinct radial locations at which there are such chains [see Fig. 1(b)].

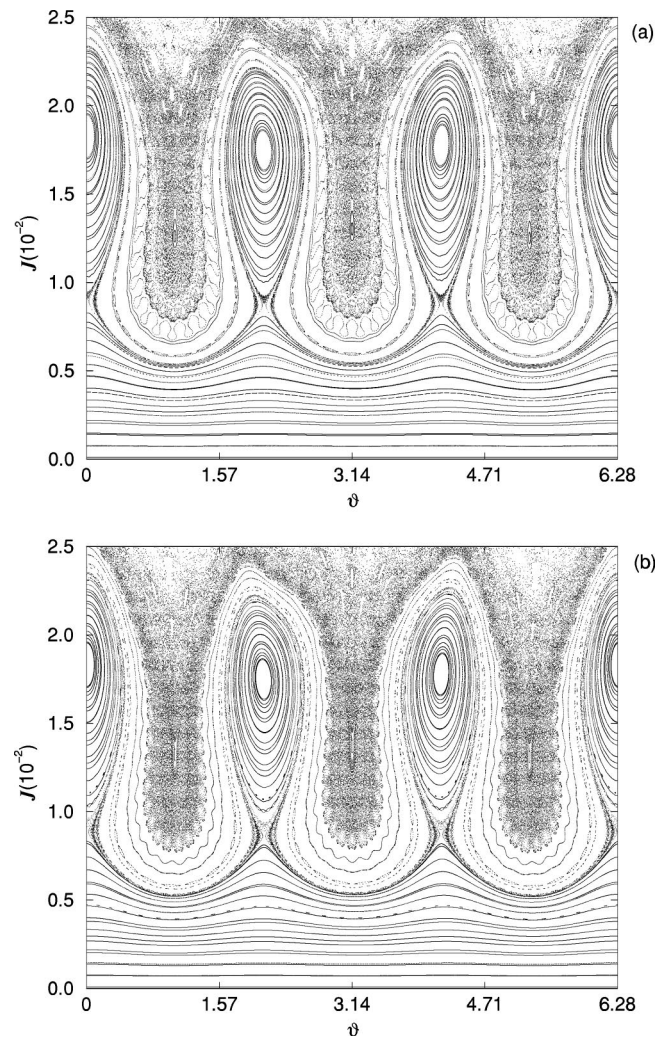


FIG. 4. Poincaré maps for the ergodic limiter mapping, an equilibrium with $\beta=3.0$ and $\gamma=1.0$, and normalized limiter currents $I_h/I_p=(a)$ 5.56% and (b) 5.81%, respectively, before and at the bifurcation.

As we approach the point at which $q(r)$ is a minimum, these island chains approach each other and eventually coalesce into a single chain in a smooth fashion. This is possible provided the two chains are arranged such that the order of the fixed points is alternate for the chains—an elliptic point of one has the same angular position of a hyperbolic point of the other and vice versa [Fig. 3(a)]. Increasing the perturbation current, field line reconnection occurs at a critical value $I_h/I_p=1.15\%$ [see Fig. 3(b)]. We will refer as the upper and lower chains, those islands with higher and lower values of the action at their centers, respectively. The topology of the field lines is changed after reconnection: there appear new open curves, or meanders, which are able to explore both chains [Fig. 3(c)]. These curves are not preexistent in the set of safety factor before the perturbation, and are born through a mechanism described in detail (for general nontwist maps) in Ref. 11.

As we increase the perturbation strength $\epsilon \sim I_h$ the islands become wider [Fig. 4(a)]. However, since the island chains are no longer pendular in a reversed shear configuration, for the ergodic limiter map is non-twist, the island

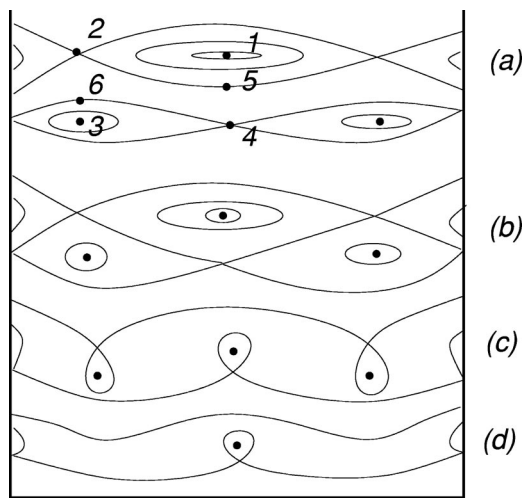


FIG. 5. Schematic figure showing dimerized island structure and fixed points (a) before, (b) during, and (c) after reconnection, and (d) after bifurcation.

width does not necessarily grow with the perturbation strength in a square-root way as it does in twist maps.⁹ Moreover, since we are dealing with a non-integrable system, we also have a chaotic layer surrounding the island separatrices, and whose width also increases with ϵ . This effect is more pronounced for the upper chain [Fig. 4(a)].

We stress here that the reconnection process here described is not due to small dissipative effects caused by a resistive layer, but instead is a rigorously flux-preserving process in which the number and the index of the fixed points of a field line map remain the same, but with a new arrangement for the map trajectories. When the perturbation strength is further increased, the elliptic point first approaches a hyperbolic point in the lower dimerized chain [Fig. 4(a)]. At $I_h/I_p = 5.81\%$ these points coalesce and disappear through a saddle-center bifurcation [Fig. 4(b)], leaving only open trajectories for the upper chain.³⁰

Figure 5 represents schematically the sequence of events, as the perturbation strength is increased, from top to bottom. Before the reconnection [Fig. 5(a)] there are two distinct island chains, from which we call **1** and **2**, the elliptic and hyperbolic points of the upper chain; **3** and **4** are the elliptic and hyperbolic points of the lower chain, respectively. We denote as **5** and **6** the lowest and highest points (in terms of the action variable) of the upper and lower islands, respectively. Exactly at the reconnection point, for which the control parameter I_h reaches a critical value $(I_h)_R$, both chains are glued up [Fig. 5(b)], so that the hyperbolic points of the neighbor chains (**2** and **4**) are joined by smooth lines. As a consequence, the points belonging to the pairs marked **2-6** and **4-5** join together. After the reconnection occurs, some of the closed curves surrounding the elliptic points **1** and **3** remain so, and open curves, or meanders, are created [Fig. 5(c)].³¹ The remaining closed curves are now bounded by separatrices which self-intercept at the former points **2** (for the upper chain), and **4** (for the lower chain). As the control parameter continues to increase, the points **2-3** approach each other and coalesce at a second critical value

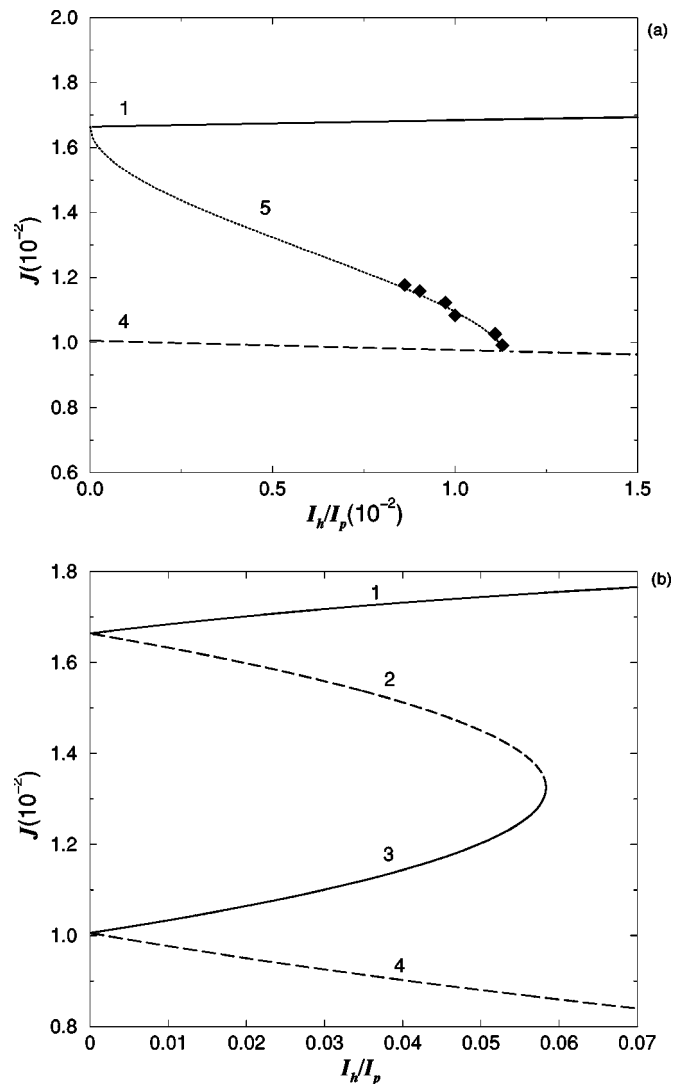


FIG. 6. (a) Reconnection diagram showing the evolution of the fixed point locations (in action space) with respect to the normalized limiter current; (b) bifurcation diagram for the fixed point locations. In both diagrams, full and dashed lines indicate stable and unstable fixed points, respectively.

$(I_h)_B$, due to a saddle-center bifurcation [Fig. 5(d)]. Meanwhile, the other pair (**1-4**) survives the bifurcation, at least for this perturbation strength.

In order to determine the critical perturbation amplitude for reconnection and bifurcation, we have plotted in Fig. 6(a) the values of the action corresponding to the points named **1**, **4**, and **5** in Fig. 5 versus the normalized perturbation current. The solid and dashed lines were obtained from Eqs. (20)–(22), whereas the dotted line was obtained by using an approximated local Hamiltonian, to be presented in the next section, while the squares correspond to values obtained from Eqs. (20)–(22). The occurrence of reconnection means that the curves corresponding to the points **4** and **5** cross each other, which happens for $(I_h)_R/I_p = 1.15\%$. Figure 6(b) shows similar results for points **1**, **2**, **3**, and **4**, where the action values were obtained from Eqs. (20)–(22). In this Fig. 6(b), the bifurcation occurs when the curves corresponding to the points **2** and **3** intercept each other, at $(I_h)_B/I_p = 5.81\%$. These critical values are expected to modify as the

equilibrium parameters are likewise changed. We have verified that the ratio $(I_h)_B/I_p$ increases by a factor lying between 10% and 60%, when the safety factor at plasma edge $q(a)$ builds up from values around 4.0. In other words, it becomes much more difficult to obtain reconnection, for higher $q(a)$, due to increasing separations of the dimerized islands.

IV. LOCAL HAMILTONIAN DESCRIPTION FOR DIMERIZED ISLANDS

The fact that the magnetic shear presents a reversal of sign inside the plasma makes the field line map derived at the end of the previous section a non-twist one. This means that KAM theory does not apply, and some results concerning formation and behavior of periodic islands cannot be used directly. One of the noteworthy points is that the islands are no longer of a pendular shape, like in the monotonic shear case. Moreover, the Chirikov scenario for explaining chaos as the overlapping of resonances is no longer valid, since the island chains reconnect rather than merge their chaotic layers.

However, as long as we limit ourselves to a small perturbation amplitudes, we can analyze how islands' widths increase with the limiter current. This can be done by expanding the field line Hamiltonian in the vicinity of the resonant surfaces beyond the linear approximation, i.e., by taking into account higher order terms due to the non-pendular nature of the periodic islands. The result can be used to estimate the critical perturbation amplitude necessary for field line reconnection and, consequently, island dimerization.

We begin from the Hamiltonian (19), and use the Fourier expansion of the periodic delta function to rewrite it in the following form:²⁵

$$H(\mathcal{J}, \vartheta, t) = H_0(\mathcal{J}) + \epsilon \sum_{s=-\infty}^{+\infty} \left(\frac{r_t}{b_t} \right)^{m_0} \cos[m_0 \vartheta - (n_0 + sN_r)t]. \quad (25)$$

We pick up from the expression above only the resonant term with frequency $\omega_0(\mathcal{J}_1) = \omega_0(\mathcal{J}_2) = n_0/m_0$, for it is responsible for the formation of the island chains to be analyzed. Expanding the result in a Taylor series around either one of the points $\mathcal{J}^* = \mathcal{J}_i$, $i = 1, 2$, and dropping the constant terms, we obtain

$$H \approx \omega_0(\mathcal{J}^*) \Delta \mathcal{J} + \frac{1}{2} \frac{d\omega_0}{d\mathcal{J}} \Big|_{\mathcal{J}=\mathcal{J}^*} (\Delta \mathcal{J})^2 + \frac{1}{6} \frac{d^2\omega_0}{d\mathcal{J}^2} \Big|_{\mathcal{J}=\mathcal{J}^*} (\Delta \mathcal{J})^3 + \epsilon \left(\frac{r_t}{b_t} \right)^{m_0} \cos(m_0 \vartheta - n_0 t),$$

where

$$\Delta \mathcal{J} = \mathcal{J} - \mathcal{J}^*. \quad (26)$$

This expression can be further simplified by making a canonical transformation to new action-angle variables $(\mathcal{J}', \vartheta')$ which eliminates the explicit time dependence, which can be done through the generating function

$$S(\mathcal{J}', \vartheta, t) = \left(\vartheta - \frac{n_0}{m_0} t \right) \mathcal{J}', \quad (27)$$

leading to the autonomous Hamiltonian

$$H'(\mathcal{J}', \vartheta') = \frac{M}{2} \mathcal{J}'^2 - \frac{W}{3} \mathcal{J}'^3 + K \cos(m_0 \vartheta'), \quad (28)$$

in which we have introduced the following abbreviations:

$$M(\mathcal{J}^*) \equiv \frac{d\omega_0}{d\mathcal{J}} \Big|_{\mathcal{J}=\mathcal{J}^*}, \quad W(\mathcal{J}^*) \equiv \frac{1}{2} \frac{d^2\omega_0}{d\mathcal{J}^2} \Big|_{\mathcal{J}=\mathcal{J}^*}, \quad (29)$$

$$K(\mathcal{J}^*) \equiv \epsilon \left(\frac{r_t}{b_t} \right)^{m_0}.$$

Notice that, if $W=0$, the Hamiltonian reduces to that of a nonlinear pendulum, which is the standard procedure used in secular perturbation theory to describe the phase-space structure near a given resonance.⁹ Due to the nonpendular character of the dimerized islands, however, we have to include a cubic term in the Taylor expansion, which turns to be a better approximation. The Hamilton equations corresponding to the quasipendular Hamiltonian (28) are written as

$$\frac{d\mathcal{J}'}{dt} = m_0 K \sin(m_0 \vartheta'), \quad (30)$$

$$\frac{d\vartheta'}{dt} = \mathcal{J}'(M - W\mathcal{J}'). \quad (31)$$

The equilibrium points of the above two-dimensional system of equations are $(\mathcal{J}^* = 0, \vartheta' = \ell \pi / m_0)$ and $(\mathcal{J}^* = M/W, \vartheta' = \ell \pi / m_0)$, with $\ell = 0, 1, 2, \dots$. For $\mathcal{J}^* = 0$ and ℓ even (odd) integers, these fixed points are hyperbolic (elliptic), or linearly unstable (neutrally stable). For the points with $\mathcal{J}^* = M/W$ the stability properties are just interchanged. Unlike the original field line Hamiltonian (19), which includes all the infinite modes generated by the perturbation and thus is nonintegrable, the reduced Hamiltonian (28) is explicitly integrable. A phase portrait obtained from (28) would reveal, as expected, two dimerized island chains, due to the exchange of stability occurring for different values of the action \mathcal{J}^* . Expanding in the neighborhood of the lower chain, i.e., taking $\mathcal{J}^* = \mathcal{J}'_1$, the island width agrees with the numerical results, whereas the other twin island would have widths considerably less than those numerically observed. If we expand instead around $\mathcal{J}^* = \mathcal{J}'_2$, the agreement now is for the upper chain.

Besides predicting the widths of each dimerized island, we can use the reduced Hamiltonian (28) to make an estimation of the critical value of the limiter current necessary to reconnection. Remember, from Fig. 5, that the critical current $(I_h)_R$ is such that the width of one of the islands is equal to the distance between the elliptic point of this island and the corresponding hyperbolic point of the other dimerized island. On applying the invariant (28), it turns out that the width of an island, $x = (\Delta \mathcal{J}')_{\max}$, is a real and positive root of the equation

$$x^3 - \frac{3}{2} \frac{M}{W} x^2 + 6 \frac{M}{W} = 0. \quad (32)$$

Let us assume that such a parameter exists. Rewriting the perturbation amplitude as $K = \zeta K_c$, where $0 < \zeta < 1$ is a tunable parameter, and $K_c \equiv M^3 / (12W^2)$, there results

$$x = \frac{1}{2} \left| \frac{M}{W} \right| \left| 2 \cos\left(\frac{\phi + \pi}{3}\right) - 1 \right|, \quad (33)$$

in which $\phi = \cos^{-1}(1 - 2\zeta)$.

Equating x to the distance $|\mathcal{J}'_1 - \mathcal{J}'_2|$ between the elliptic and hyperbolic points of different chains we obtain a transcendental equation, the numerical solution of which gives a threshold for ζ and, from (29), critical current for reconnection. In particular, for the same parameters used to plot the numerical Poincaré maps of the previous section, the critical I_h/I_p for reconnection is estimated to lie between 1.07% and 1.14%, which compares well to the numerical one, namely, 1.15% [see Fig. 3(b)].

V. TRANSPORT BARRIER

The formation of dimerized island chains when a resonant external perturbation acts on a tokamak equilibrium with reversed shear has a profound effect on the transport properties of chaotic field lines. In order to generate the latter, the field line system has to be nonintegrable, which is provided by the explicit φ dependence of the limiter field. For limiter perturbations acting on an equilibrium with a monotonic safety factor, the properties of the related chaotic region have been studied.^{25,32} KAM theory and global stochasticity criteria allow us to determine the onset of large-scale chaotic behavior, as well as the size of the chaotic region, also permitting us to investigate field line diffusion.³³

In the case of a reversed shear equilibrium, we also expect the formation of a peripheric chaotic region, but island reconnection influences field line diffusivity, as illustrated by Figs. 7(a) and 7(b), showing phase portraits of situations without and with reversed shear, respectively, and a high limiter current. The differences in the observed concentration of orbit points in the chaotic regions suggest that there has been formed a transport barrier which creates an obstacle to field line diffusion in the chaotic region, since chaotic field lines near islands' separatrices are trapped for a finite time-span in this barrier before escaping.

In order to verify numerically this observation, we have analyzed field line diffusivity by taking a large number N_ϑ of initial conditions uniformly spread along the chaotic region, for a constant \mathcal{J} and a large number of poloidal angles $\vartheta_{0i} = 2\pi i / N_\vartheta$, with $i = 1, 2, \dots, N_\vartheta$. The mean size of the radial excursions a field line undergo in the chaotic region can be quantified by the average quadratic deviation of the action variable

$$\sigma_n^2 \equiv \langle (\delta \mathcal{J}_n)^2 \rangle_i = \frac{1}{N_\vartheta} \sum_{i=1}^{N_\vartheta} (\mathcal{J}_{ni} - \mathcal{J}_{0i})^2, \quad (34)$$

which, under fairly general assumptions, goes asymptotically with the discrete time as a power-law n^μ .³⁴ Anomalous transport is characterized by $\mu \neq 1$, which we call sub-(super-) diffusive if $\mu < (>) 1$. A uniformly chaotic region is

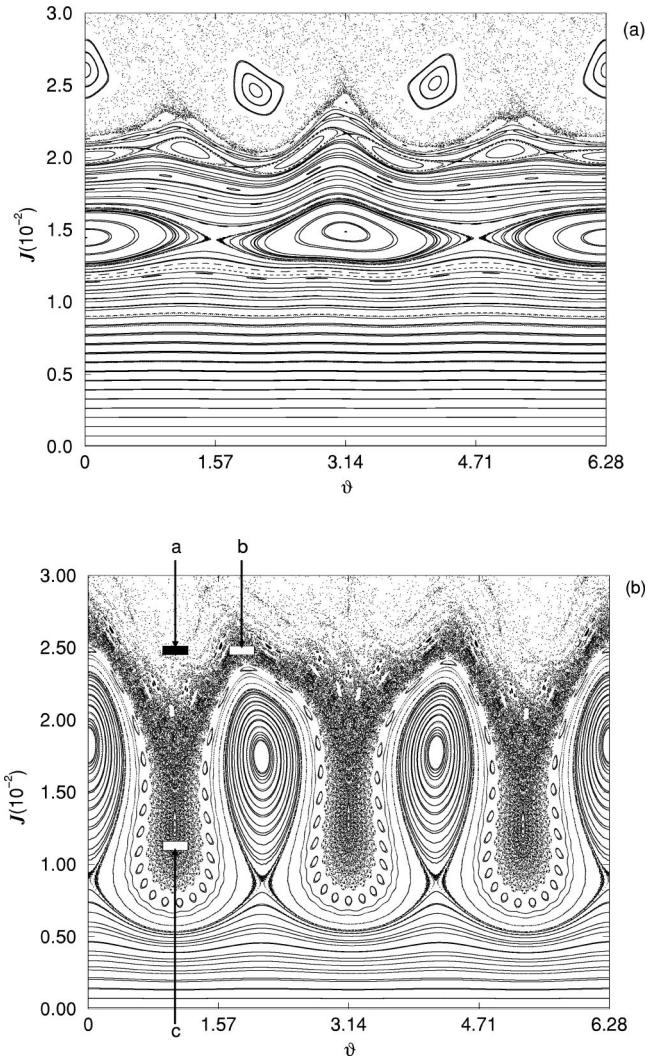


FIG. 7. Poincaré maps for the ergodic limiter mapping, for a limiter current $I_h/I_p = 5.58\%$ and equilibria with (a) $\beta = 0$ (monotonic profile) and (b) $\beta \neq 0$ (nonmonotonic profile, with reversed shear). In both cases we choose $q(a) \approx 4.0$.

characterized by Gaussian transport, for which $\mu = 1$, such that a diffusion coefficient can be defined as $D_{LF} = \lim_{n \rightarrow \infty} (1/2n) \sigma_n^2$.

Figure 8(a) shows the time evolution of the average square deviation of chaotic field lines with a high limiter current ($I_h/I_p = 5.56\%$), long after the reconnection occurs. Two sets of initial conditions were taken in two different regions: $\mathcal{J}_{0i} = 0.013$, and $\mathcal{J}_{0i} = 0.025$ for $0 \leq \vartheta_i \leq 2\pi$. One region is in the area occupied by the small dimerized islands just before the bifurcation of their fixed points (lower curve in Fig. 8). The other region is outside the surviving dimerized islands (upper curve in Fig. 8). In both cases, the overall behavior is similar for the first ten map iterations: σ_n^2 increases in a superdiffusive way (with μ between 1.6 and 1.8). After that, for the next 100 iterations, the outside region shows an almost diffusive expansion ($\mu \approx 0.9$), while the internal region is still superdiffusive ($\mu \approx 2.2$). The quadratic deviation tends to stabilize, yet with some rippling, for the subsequent map iterations.

The non-Gaussian nature of the transport regimes shown

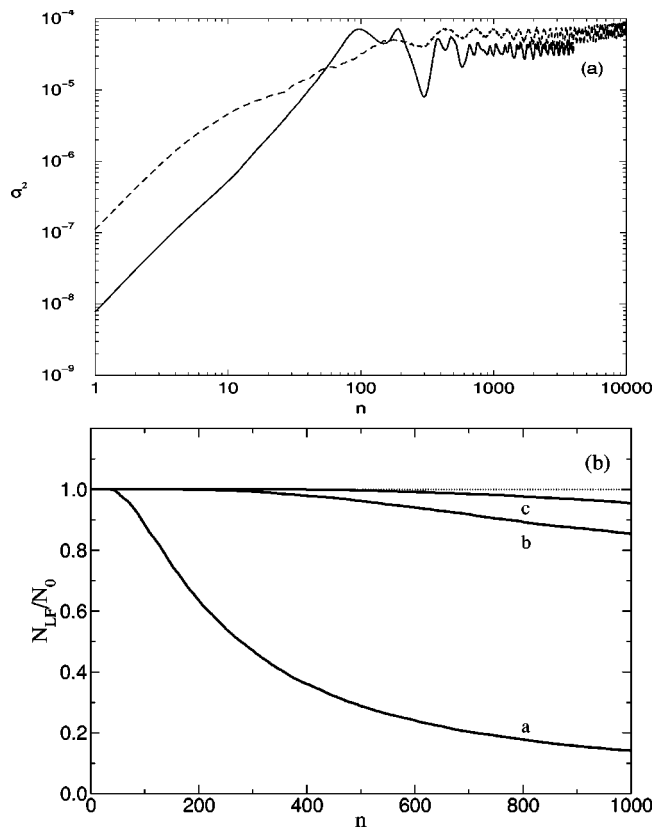


FIG. 8. (a) Average quadratic deviation with $\beta=3.0$, $\gamma=1.0$, limiter currents $I_h/I_p=5.56\%$, and initial conditions centered at $\mathcal{J}_0=0.013$ (lower curve) and 0.025 (upper curve). (b) Fraction of lost field lines for the same parameters and $N_0=10\,000$. The initial conditions were picked up from the boxes named **a**, **b**, and **c** of Fig. 7(b).

in Fig. 8(a) can be understood by two basic reasons. First, the superdiffusive explosion for small times is explained by the existence, within the chaotic region, of “escape channels,” through which field lines run away very fast and eventually collide with the tokamak wall. These channels result from the homoclinic tangle of invariant manifolds stemming from hyperbolic fixed points embedded in the chaotic region.³⁵ Second, the apparent saturation of σ_n^2 is due to a trapping effect on the field lines caused by the existence of undestroyed periodic islands embedded in the chaotic region. A chaotic field line that approaches the remnant of an island would stay around it for a given time before entering in the neighborhood of another island, and so on (“stickiness” of trajectories).³⁶

Since the chaotic region produced by an ergodic limiter is supposed to reach the tokamak wall, virtually all chaotic field lines eventually hit the wall. In this case we stop the map iterations and consider the field line as being lost.^{33,37} The slower the field line decay is, the most effective turns to be the diffusion barrier created in the region immediately above the dimerized island. In Fig. 8(b) we plot the number of the remaining field lines after n map iterations, for three sets of initial conditions picked up from the boxes drawn in Fig. 7(b). Box **a** was chosen from a region outside the transport barrier, while box **b** was within the transport barrier, as well as the third box (**c**), which was chosen inside the chaotic

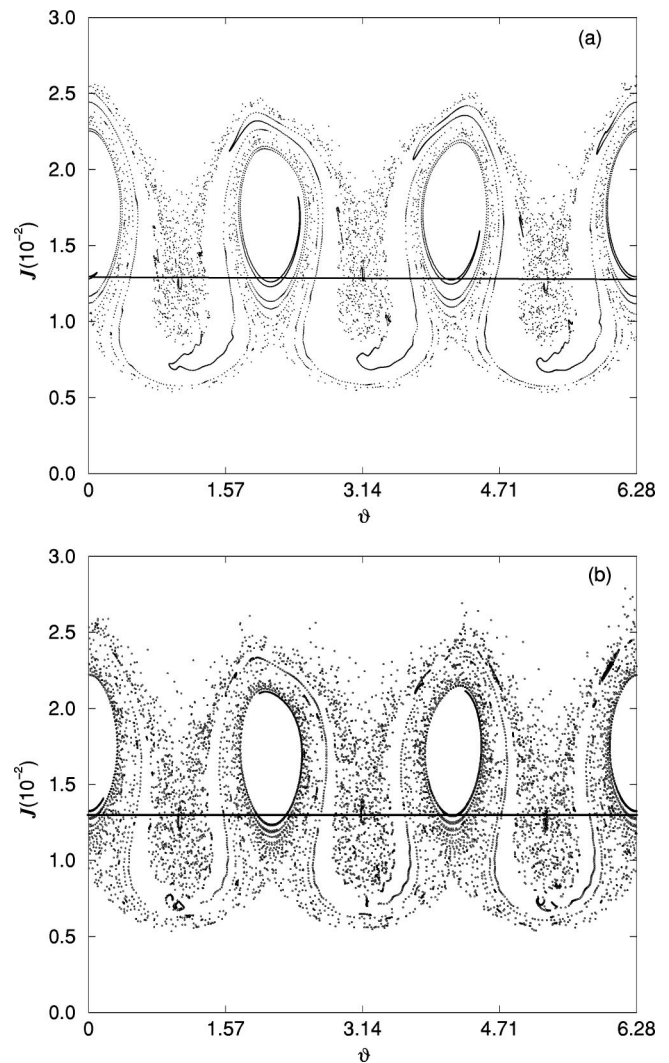


FIG. 9. Image of a line of 10^4 initial conditions after (a) 300 and (b) 1000 iterations of the ergodic limiter map, with $I_h=5.58\%$ of the plasma current.

region between the islands. In the case of **a**, we have verified an exponential dependence for the number of remaining field lines, but without noticeable decay for the cases **b** and **c**, corresponding to initial conditions placed in the two boxes within the transport barrier. We have considered a large number of toroidal turns, but we plot in Fig. 8(b) only a small number of them, compatible with the typical duration of a tokamak discharge.

Field line diffusion in the peripheric chaotic region formed by a limiter is not uniform, and it strongly influenced by the invariant manifolds belonging to the unstable fixed points embedded in the chaotic region. Invariant manifolds are sets of points whose forward and/or backward iterations belong to the same set. For stable (unstable) manifolds, forward (backward) iterates converge, as n goes to infinity, to a hyperbolic fixed point.³⁸ The chaotic region itself results from an infinite number of intersections between manifolds belonging to different unstable fixed points.⁹ Moreover, embedded in these chaotic layers, we found many small higher-order islands, and field lines stick temporarily to the region around them. Figure 9 illustrates this fact, depicting the for-

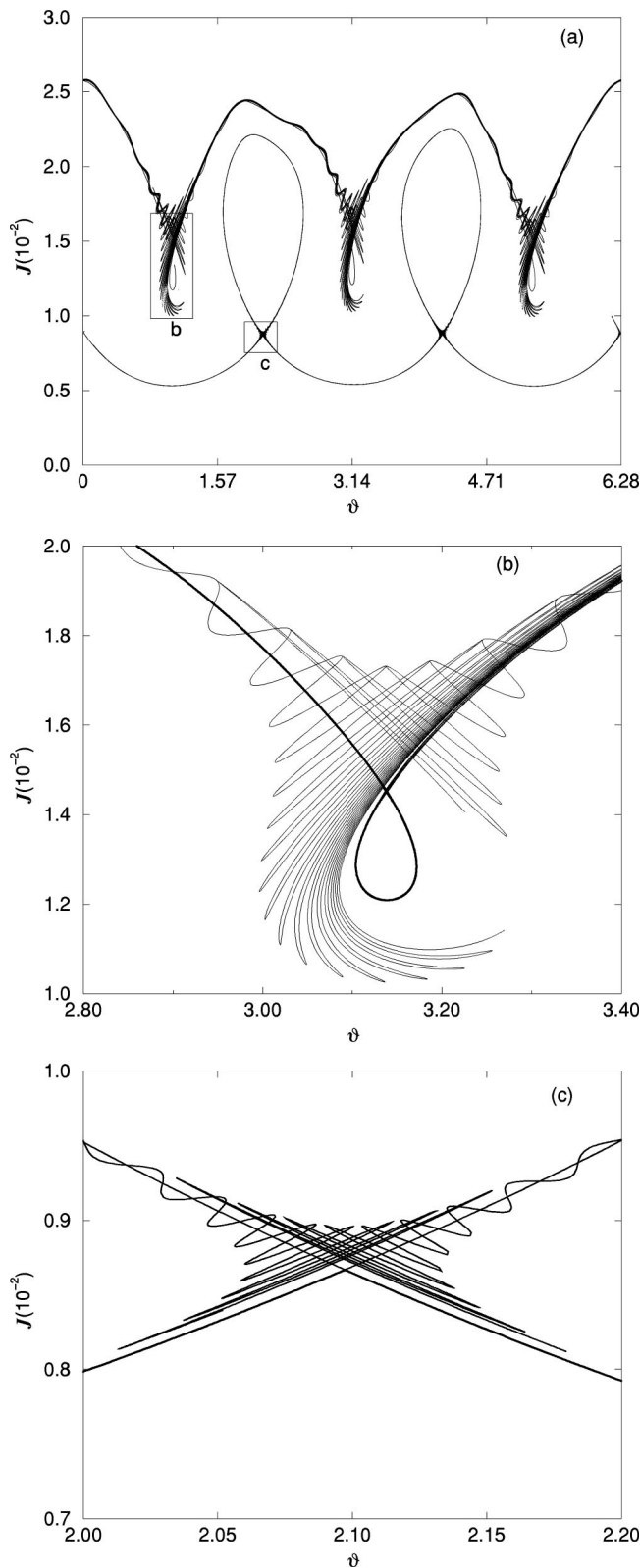


FIG. 10. (a) Unstable manifolds of the hyperbolic point, as shown by the Poincaré map with $I_h/I_p=5.58\%$. (b) and (c) are magnifications of selected portions of the figure.

ward images, under the ergodic limiter map, of a line of initial conditions after 300 and 1000 iterations, respectively. Most of the orbit points follows approximately the invariant manifolds stemming from the unstable fixed points embed-

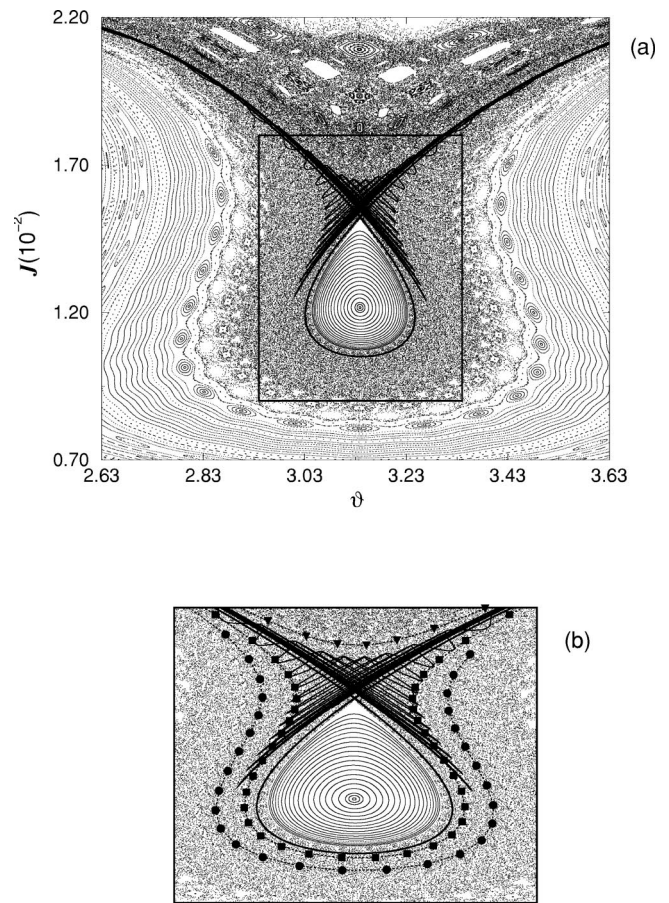


FIG. 11. (a) Magnification of a trapping region in the Poincaré map with $I_h/I_p=4.75\%$ around a hyperbolic point of the lower chain; (b) zoom of the rectangle shown in (a) depicting successive iterations (using circles, squares, and triangles) of one trapped orbit before it escapes. Both figures exhibit the crossings between stable and unstable manifolds.

ded in the chaotic layer near the shearless region.

Figure 9 reveals two trapping regions structured around hyperbolic fixed points with unequal widths. The most pronounced trapping region is related to the hyperbolic points of the lower dimerized chain. This can be understood in terms of the crossings of the invariant manifolds, as can be observed in Fig. 10(a). The crossings related to the lower chain [Fig. 10(b)] fill up a larger area, compared with the crossings area for the upper chain [Fig. 10(c)]. This trapping effect persists even after the bifurcation, as one can see by comparing Figs. 4(a) and 4(b), hence, this effect is quite robust for increasing perturbing resonance amplitude, in agreement with the experimental results.¹⁻⁴

The trapping effect is more effective in the chaotic region of the Poincaré map around the hyperbolic point. In order to show that, we present in Fig. 11(a) a magnification of this region for $I_h/I_p=4.75\%$, together with the manifold crossings. In Fig. 11(b) we show an iteration sequence of a temporarily trapped orbit before it leaves the mentioned chaotic region. Points marked as circles in Fig. 11(b) appear in first place, and then squares, followed by triangles. Hence, this orbit follows successive layers while drifting slowly from one layer to another. The slow motion is mainly determined by the manifold crossings. Thus, after staying for a

large number of iterations in the region bounded by the cantori around the hyperbolic point, the trapped orbit finally goes outwards leaving the low-shear barrier. This process has been analyzed also for other conservative maps.^{36,39,40} Hence, our transport barrier is only partially effective to hampers field line diffusion, since it exists due to the stickiness effect of the magnetic island boundaries on chaotic field lines and not due to a limited chaotic region bounded by an undestroyed magnetic surface. This field line stickiness is effective, however, for a timescale much larger than the typical tokamak discharge duration.

VI. CONCLUSIONS

In this paper we have used an analytically obtained field line map to investigate the effects of an ergodic magnetic limiter on the magnetic field line structure which results from using a reversed magnetic shear. The main result is the creation of an outer chaotic layer which traps the field lines. This layer works like an effective transport barrier, with respect to the typical plasma duration. The trapping is more effective around the shearless plasma. It should be stressed that the barrier could only be observed due to the non-monotonic character of the safety factor, when combined with the effect of an ergodic magnetic limiter. This barrier is created from a small chaotic region, due to the localized action of the ergodic limiter, and results basically from the properties of field line trajectories in the vicinity of separatrices of islands bordering the chaotic region. Hence, it turns out that this transport barrier is somewhat different from that considered in Ref. 12, where the barrier arises from a large chaotic region. Finally, previous works on the formation of transport barriers from reversed shear profiles have focused on internal modes as the sources of nonintegrability leading to field line chaos. Here, on the other hand, the chaotic region results from an external device (the ergodic limiter) in such a way we could reproduce and perhaps control conditions leading to plasma instability in tokamak discharges, which would lead to a better understanding of the conditions under which tokamak confinement can be substantially improved.

ACKNOWLEDGMENTS

This work was made possible with partial financial support of the following agencies: CNPq, CAPES, FAPESP, and Fundação Araucária.

APPENDIX: EXPLICIT FORM OF THE FIELD LINE MAPPING FOR AN ERGODIC LIMITER

Under the restriction $r_t/R'_0 < 1/2$, as discussed in Sec. II, we introduce action-angle variables, which are related to the spatial coordinates by:²⁵

$$\mathcal{J}(r_t) = \frac{1}{2\pi R'_0 B_T} \int \mathbf{B}_0 \cdot d\sigma_3 = \frac{1}{4} \left[1 - \left(1 - 4 \frac{r_t^2}{R_0'^2} \right)^{1/2} \right], \quad (\text{A1})$$

$$\begin{aligned} \vartheta(r_t, \theta_t) &= \frac{1}{q(r_t)} \int_0^{\theta_t} \frac{B_0^3(r_t, \theta_t)}{B_0^2(r_t, \theta_t)} d\theta \\ &= \left[1 - 4 \left(\frac{r_t}{R'_0} \right)^2 \right]^{1/2} \int_0^{\theta_t} \frac{d\theta}{1 - 2 \frac{r_t}{R'_0} \cos \theta} \\ &= 2 \arctan \left[\frac{1}{\Omega(r_t)} \left(\frac{\sin \theta_t}{1 + \cos \theta_t} \right) \right] \end{aligned} \quad (\text{A2})$$

where $d\sigma_3 = R'_0 r_t dr_t d\theta_t \hat{e}^3$ and

$$\Omega(r_t) = \left(1 - 2 \frac{r_t}{R'_0} \right)^{1/2} \left(1 + 2 \frac{r_t}{R'_0} \right)^{-1/2}. \quad (\text{A3})$$

We remark that $\mathcal{J}(r_t) \geq 0$ for any $r_t \geq 0$. $q(r_t)$ is the safety factor, given by (12), and with a nonmonotonic profile, provided we choose plasma current profiles like (8).

With help of these canonically conjugate variables, we write the perturbation term in the Hamiltonian (19) as

$$H_1(\mathcal{J}, \vartheta, t) = \sum_{m'=0}^{2m_0} H_{m'}[r_t(\mathcal{J})] e^{i[m' \theta_t(\mathcal{J}, \vartheta) - n_0 t]}, \quad (\text{A4})$$

where the coefficients are

$$H_{m'}(r_t) = -J_{m'-m_0}(m_0 \lambda) \left(\frac{r_t}{b_t} \right)^{m'}. \quad (\text{A5})$$

The Fourier expansion of the perturbation Hamiltonian in the angle variables furnishes

$$H_1(\mathcal{J}, \vartheta, t) = \sum_{n=0}^{2m_0} H_n^*(\mathcal{J}) e^{i(n\vartheta - n_0 t)}, \quad (\text{A6})$$

with Fourier coefficients given by

$$H_m^*(\mathcal{J}) = \sum_{m'=0}^{2m_0} H_{m'}[r_t(\mathcal{J})] S_{m,m'}(\mathcal{J}), \quad (\text{A7})$$

and the following quantities have been defined:

$$\begin{aligned} S_{m,m'}(\mathcal{J}) &= (-1)^m \left(\frac{c_1(\mathcal{J})}{c_2(\mathcal{J})} \right)^{m+m'} \\ &\quad \times \sum_{n=0}^m (-1)^n \alpha_n(m, m') \left(\frac{c_1(\mathcal{J})}{c_2(\mathcal{J})} \right)^{-2n}, \end{aligned} \quad (\text{A8})$$

with

$$c_1(\mathcal{J}) = 1 - \frac{1}{\Omega[r_t(\mathcal{J})]}, \quad (\text{A9})$$

$$c_2(\mathcal{J}) = 1 + \frac{1}{\Omega[r_t(\mathcal{J})]}, \quad (\text{A10})$$

$$\alpha_n(m, m') = \begin{cases} 1 & \text{if } m=0 \text{ and } n=0, \\ m' & \text{if } m=1 \text{ and } n=0 \text{ or } n=1, \\ m' \frac{(m+m'-n-1)!}{(m-n)!(m'-n)!n!} & \text{if } m>1 \text{ and } n \leq m', \\ 0 & \text{if } m>1 \text{ and } n > m'. \end{cases} \quad (\text{A11})$$

The functions $f(\mathcal{J}, \vartheta, t)$ and $g(\mathcal{J}, \vartheta, t)$, appearing in the map Eqs. (20)–(22), are obtained by differentiation of (A6) with respect to ϑ and \mathcal{J} , respectively.

-
- ¹F. M. Levinton, M. C. Zarnstorf, S. H. Batha *et al.*, Phys. Rev. Lett. **75**, 4417 (1995).
²E. J. Strait, L. L. Lao, M. E. Manel *et al.*, Phys. Rev. Lett. **75**, 4421 (1995).
³E. Mazzucato, S. H. Batha, M. Beer *et al.*, Phys. Rev. Lett. **77**, 3145 (1996).
⁴For a recent collection of papers on many experimental aspects of reversed shear configurations in large tokamaks see the special issue of Plasma Phys. Controlled Fusion **44** (7) (2002).
⁵D. Robinson, Nucl. Fusion **25**, 1101 (1985).
⁶J. E. Howard and S. M. Hohns, Phys. Rev. A **29**, 418 (1984).
⁷D. Castillo-Negrete, J. M. Greene, and P. J. Morrison, Physica D **91**, 1 (1996).
⁸P. J. Morrison, Phys. Plasmas **7**, 2279 (2000).
⁹A. J. Lichtenberg and M. A. Lieberman, *Regular and Chaotic Dynamics*, 2nd ed. (Springer, New York, 1992).
¹⁰R. Balescu, Phys. Rev. E **58**, 3781 (1998).
¹¹E. Petrisor, J. H. Misguich, and D. Constantinescu, Chaos, Solitons Fractals **18**, 1085 (2003).
¹²G. Corso and F. B. Rizzato, Phys. Rev. E **58**, 8013 (1998).
¹³D. Dimock and H. Johnson, Nucl. Fusion **13**, 271 (1973); K. Makishima, T. Tominaga, H. Toyuama, and S. Yoshikawa, Phys. Rev. Lett. **36**, 142 (1976).
¹⁴W. Kerner and H. Tasso, Phys. Rev. Lett. **49**, 654 (1982).
¹⁵F. Karger and F. Lackner, Phys. Lett. **A61**, 385 (1977).
¹⁶W. Engelhardt and W. Feneberg, J. Nucl. Mater. **76/77**, 518 (1978).
¹⁷W. Feneberg and G. H. Wolf, Nucl. Fusion **27**, 669 (1981).
¹⁸T. J. Martin and J. B. Taylor, Plasma Phys. Controlled Fusion **26**, 321 (1984).
¹⁹S. C. McCool, A. J. Wootton, A. Y. Aydemir *et al.*, Nucl. Fusion **29**, 547 (1989).
²⁰K. H. Dippel, J. Nucl. Mater. **147**, 3 (1987).
²¹J. C. Vallet, L. Poutchy, M. S. Mohamed-Benkadda *et al.*, Phys. Rev. Lett. **67**, 2662 (1991).
²²I. L. Caldas, R. L. Viana, M. S. T. Araujo *et al.*, Braz. J. Phys. **32**, 980 (2002).
²³M. Y. Kucinski and I. L. Caldas, Z. Naturforsch., A: Phys. Sci. **42**, 1124 (1987).
²⁴M. Y. Kucinski, I. L. Caldas, L. H. A. Monteiro, and V. Okano, J. Plasma Phys. **44**, 303 (1990).
²⁵E. C. da Silva, I. L. Caldas, and R. L. Viana, IEEE Trans. Plasma Sci. **29**, 617 (2001).
²⁶P. M. Morse and H. Feshbach, *Methods of Theoretical Physics* (McGraw-Hill, New York, 1953), Vol. 2.
²⁷G. A. Oda and I. L. Caldas, Chaos, Solitons Fractals **5**, 15 (1995); G. Corso, G. A. Oda, and I. L. Caldas, *ibid.* **8**, 1891 (1997).
²⁸R. L. Viana and D. B. Vasconcelos, Dyn. Stab. Syst. **12**, 75 (1997).
²⁹I. L. Caldas, J. M. Pereira, K. Ullmann, and R. L. Viana, Chaos, Solitons Fractals **7**, 991 (1996).
³⁰M. Ding, C. Grebogi, E. Ott, and J. A. Yorke, Phys. Rev. E **42**, 7025 (1990).
³¹E. Petrisor, Chaos **11**, 497 (2001).
³²E. C. da Silva, I. L. Caldas, and R. L. Viana, Chaos, Solitons Fractals **14**, 403 (2002).
³³E. C. da Silva, I. L. Caldas, and R. L. Viana, Phys. Plasmas **8**, 2855 (2001).
³⁴J. D. Meiss, Rev. Mod. Phys. **64**, 796 (1992).
³⁵E. C. da Silva, I. L. Caldas, R. L. Viana, and M. A. F. Sanjuan, Phys. Plasmas **9**, 4917 (2002).
³⁶J. H. Misguich, J. D. Reuss, D. Constantinescu, G. Steinbrecher, M. Vlad, F. Spineanu, B. Weyssow, and R. Balescu, Plasma Phys. Controlled Fusion **44**, L29 (2002).
³⁷J. E. S. Portela, R. L. Viana, and I. L. Caldas, Physica A **317**, 411 (2003).
³⁸E. Ott, *Chaos in Dynamical Systems* (Cambridge University Press, Cambridge, U.K., 1994).
³⁹R. S. MacKay, J. D. Meiss, and I. C. Percival, Phys. Rev. Lett. **52**, 697 (1984).
⁴⁰C. Efthymiopoulos, G. Contopoulos, N. Voglis, and R. Dvorak, J. Phys. A **30**, 8167 (1997).